Nanoscale
Advances

PAPER

View Article Online
View Journal | View Issue

Check for updates

Cite this: *Nanoscale Adv.*, 2020, **2**, 3550

2D AuPd alloy nanosheets: one-step synthesis as imaging-guided photonic nano-antibiotics†

Songliang He,‡[a] Guoshuai Zhu,‡[a] Zhencheng Sun,[a] Jidong Wang,[bc] Ping Hui,[a] Penghe Zhao,[a] Wenwen Chen *[ac] and Xingyu Jiang [d]

Received 30th April 2020
Accepted 25th June 2020

DOI: 10.1039/d0na00342e

rsc.li/nanoscale-advances

The complicated synthesis and undesirable biocompatibility of nanomaterials hinder the synergistic photothermal/photodynamic therapy for bacterial infections. Herein, we develop a one-step preparation method of 2D AuPd alloy nanosheets as imaging-guided photonic nano-antibiotics. 2D AuPd alloy nanosheets with an extremely small thickness (~1.5 nm) exhibit prominent photothermal effects (η = 76.6%), excellent ROS generation, strong photoacoustic signals and desirable biocompatibility. AuPd nanosheets can eliminate 100% of representative Gram-positive (*Staphylococcus aureus*) and Gram-negative bacteria (*Escherichia coli*) when irradiated using an 808 nm laser at 1 W cm^{-2} for 5 minutes. After being modified with a bacterial targeting peptide, under the guidance of photoacoustic imaging, AuPd nanosheets achieve promising synergistic photothermal/photodynamic therapeutic efficacy in treating *Staphylococcus aureus* infected mice. This work expands the biomedical application of 2D noble metal nanomaterials to the field of photonic nano-antibiotics.

Introduction

Bacterial infections are some of the main reasons for worldwide mortality.[1] The inappropriate prescription and even the abuse of antibiotics lead to increased drug resistance.[2] Growing multiple antibiotic resistance in the face of declining antibiotic discovery is one of the most urgent health issues.[3] The boom of nanotechnology sheds light on the discovery of novel antibiotics with state-of-the-art antimicrobial activity.[4,5] However, few attempts have managed to find smart nanomaterials that specifically combat pathogenic bacteria without causing drug-resistance. Compared to the traditional medication based on antibiotics, it is less possible for photonic therapy to induce resistance as spatially confined light kills bacteria physically regardless of multidrug-resistant strains or naive ones. Since many kinds of nanomaterials have been exploited as photosensitizers, utilizing nanomaterials in photonic platforms is an ideal alternative way to fight against superbug infections.

The main approaches, photothermal therapy (PTT) and photodynamic therapy (PDT), involved in phototherapy suffer from limitations. PTT eliminates pathogens through local hyperpyrexia from light generated by nano-photothermal agents,[6] but the efficiency may expire because of higher heat-tolerance in some bacteria than healthy tissues.[7] In PDT, pathogens are eliminated by reactive oxygen species (ROS) generated from phototherapeutic agents with the help of irradiation.[8] Nonetheless, a fundamental difference is observed in PDT due to the difference in susceptibility to ROS between Gram-positive and Gram-negative strains.[9] To overcome the shortcomings of each therapeutic modality, synergistically using PTT and PDT may have a great chance to achieve excellent efficiency of pathogen destruction.[10] Additionally, the visible guidance favored by photoacoustic imaging (PAI) to realize real-time monitoring of antibacterial materials delivery is instrumental for precise photonic therapy *in vivo*. As yet, imaging-guided therapy based on targeting nanotheranostic agents in the infected region remains an open issue.[11]

Composite nanomaterials are the most common strategies for synergistic photonic therapy, but the complicated operation and poor batch-to-batch reproducibility are unavoidable.[12,13] Consequently, a one-step synthesis of nanomaterials with combined photothermal and photodynamic properties, as well as imaging-guided therapy, is highly desirable. Owing to the deep tissue penetration in the NIR region, nanostructures with NIR absorbance are the priority as light-triggered theranostic agents.[14] Among them, nanomaterials based on noble metals,[15]

---

[a] *Guangdong Key Laboratory for Biomedical Measurements and Ultrasound Imaging, School of Biomedical Engineering, Shenzhen University Health Science Center, Shenzhen 518055, China. E-mail: chenww@szu.edu.cn*

[b] *Central Laboratory, Huazhong University of Science and Technology Union Shenzhen Hospital (Nanshan Hospital), Shenzhen Nanshan People's Hospital and the 6th Affiliated Hospital of Shenzhen University Health Science Center, Shenzhen 518052, China*

[c] *John A. Paulson School of Engineering and Applied Sciences, Harvard University, Cambridge, MA 02138, USA*

[d] *Department of Biomedical Engineering, Southern University of Science and Technology, Shenzhen 518055, China*

† Electronic supplementary information (ESI) available. See DOI: 10.1039/d0na00342e

‡ Songliang He and Guoshuai Zhu contributed equally.

such as gold and palladium (Au and Pd), present advantages due to their outstanding plasmonic and catalytic properties,[16] good biocompatibility coming from chemical inertia,[17] and tunable synthetic/functionalization strategies.[18] To obtain better properties, nanostructures with the combination of Au and Pd are prepared.[19,20] Considering the tunable performance of AuPd alloys in other fields, the use of AuPd alloys in imaging-guided synergistic therapy is worth a shot.

In this study, we demonstrate a one-step process to synthesize 2D AuPd alloy nanosheets for PAI-guided PTT/PDT against pathogens (Scheme 1). Systematic optimization of synthetic protocols is implemented to get 2D AuPd nanosheets that display prominent photothermal-conversion performance, valid ROS generation ability, and a desirable photoacoustic effect under the irradiation of a single laser (808 nm). We test their antibacterial activities in the aspect of efficiency through the colony counting assay using different parameters including the concentration of AuPd, and the laser intensity and irradiation time. Under the optimized conditions, AuPd nanosheets can eliminate the overall bacteria regardless of Gram staining within minutes. In the proof-of-concept *in vivo* experiment, we coat AuPd nanosheets with the cyclic 9-amino-acid peptide CARGGLKSC[21] to realize bacteria (*Staphylococcus aureus*) targeting property, and the therapeutic utility of functionalized AuPd nanosheets under PAI is verified in mice with subcutaneous abscesses caused by *Staphylococcus aureus* (*S. aureus*).

Results and discussion

Synthesis and characterization of AuPd

We synthesize AuPd nanosheets through a one-pot chemical reduction of $HAuCl_4$ and H_2PdCl_4 in an aqueous solution of octadecyl trimethyl ammonium chloride (OTAC), with ascorbic acid as the reducing agent. The elemental proportion of reactants and dosage of the reductant are the important factors in the synthetic process. We obtained various nanostructures through adjusting the feed ratio of $HAuCl_4$ to H_2PdCl_4 and the amount of reductant (Fig. S1†). AuPd nanosheets with a feed ratio of Au : Pd (7 : 3) and a reductant amount ranging from 10 to 20 mg show the optimum morphology and photometric properties. In the following experiments, we prepare AuPd nanosheets with the optimal feed ratio of Au : Pd (7 : 3) and 10 mg of reductant. Transmission electron microscopy (TEM) photographs of AuPd nanomaterials show an anisotropic shape (length: 100–200 nm, width: ∼50 nm) (Fig. 1a and b). And a thickness of about 1.5 nm is characterized by atomic force microscopy (AFM) (Fig. 1c), suggesting a 2D sheet nanostructure. The formation of this structure is attributed to OTAC, which can act as the structure directing agent and is decisive in forming the highly anisotropic 2D structure.[22] The elemental composition is analyzed by energy-dispersive spectroscopy (EDS) combined with high-angle annular dark-field (HAADF)-scanning transmission electron microscopy (STEM), revealing that the distribution of Au and Pd has high spatial correlation

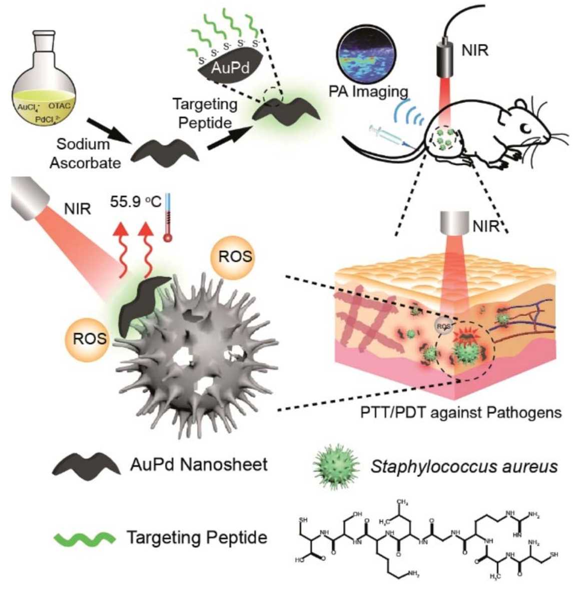

Scheme 1 Schematic (not to scale) illustration of the synthesis and modification of AuPd nanosheets, and antibacterial activities *in vivo* for the treatment of subcutaneous abscesses caused by *S. aureus*.

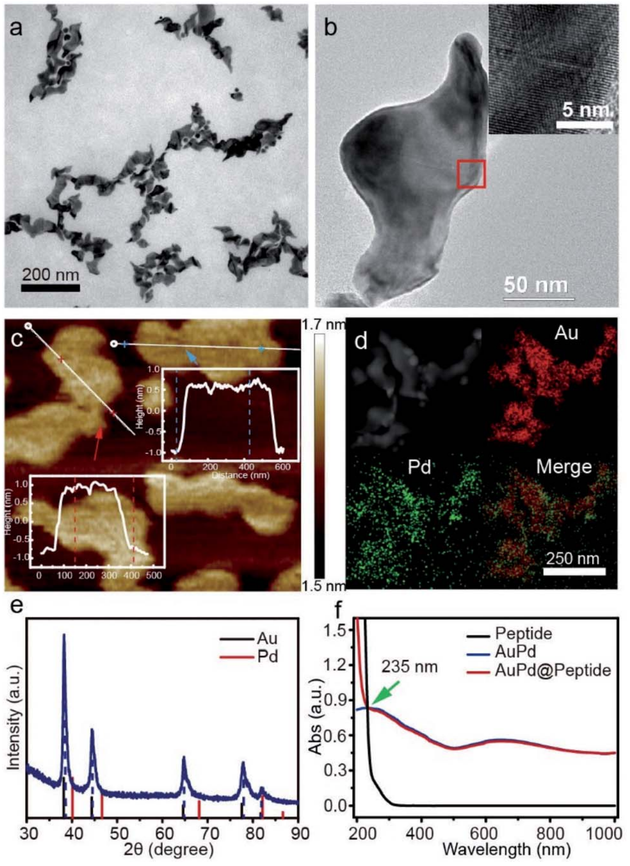

Fig. 1 Structural characterization of 2D AuPd nanosheets. (a and b) Low-resolution TEM images, inset in (b) is the high-resolution TEM images of the region enclosed by a red square. (c) AFM image and the corresponding height profile across nanosheets. (d) STEM image and the corresponding elemental mapping of Au and Pd. (e) XRD pattern of AuPd nanosheets. (f) UV-Vis absorption of AuPd, peptide, and AuPd@Peptide.

and uniform alloy nanostructures are formed (Fig. 1d). Quantitative analysis (Inductively Coupled Plasma Mass, ICP-MS) further indicates that the AuPd nanosheets consist of 78.3% Au and 21.7% Pd. Moreover, the results of high resolution TEM (HRTEM) (inset in Fig. 1b) and X-ray diffraction (XRD) (Fig. 1e) suggest a lattice diffraction pattern and a single set of diffraction peaks assignable to the face centered cubic structure located between the corresponding peaks of pure Au and pure Pd, confirming the formation of an AuPd alloy rather than phase separation.[23] We notice that the XRD pattern has only one characteristic peak for Pd, which may be attributed to the fact that the content of Au is significantly higher than that of Pd.[24]

Photothermal and photodynamic properties of AuPd

First, we characterize the optical absorption properties of AuPd nanosheets. They can absorb light in the visible and NIR regions, with the absorption peak at about 650 nm (Fig. 1f). Considering the penetration depth of laser light and only a slight difference between the absorption peak wavelength and 808 nm, in the following experiments we choose 808 nm laser light as the trigger. Since the NIR absorption endows AuPd nanosheets with potential to be used as photonic agents,[25] we investigate the photothermal conversion capabilities of AuPd nanosheets systematically. In view of the universality of 808 nm laser light and the considerable absorption of 808 nm light by AuPd nanosheets, we test the photothermal properties of different samples by exposing them to 808 nm NIR laser light, including AuPd nanosheets of different concentrations as well as pure Au or Pd nanostructures. The IR thermal images of various solutions obtained from 0 to 10 min illustrate the visual change of temperature (Fig. 2a). When the concentrations of noble metals in nanostructures are set as the same, the AuPd alloy shows better photothermal properties than pure Au or Pd nanostructures obviously (Fig. 2b). The photothermal curves of AuPd nanosheets display concentration-dependent photothermal effects (Fig. 2c). Within 10 min, the highest temperature achieved is 76.0 °C and the increase of temperature (ΔT) is 50.8 °C when the concentration of AuPd nanosheets is 50 μg mL^{-1} and the intensity of the NIR laser light is 1 W cm^{-2}, while the highest temperatures of pure Au and Pd only reach 52.1 °C and 57.2 °C under the same conditions, respectively. In sharp contrast, the highest temperature of pure water is only 29.3 °C under the same conditions. Using the same laser, to realize equal photothermal effects, significantly less AuPd nanosheets and shorter irradiation time are required for the AuPd group than those for the pure Au or Pd group. Considering their biocompatibility, their biomedical application and *in vivo* trials are meaningful. Next, we measure the heating and cooling curve of AuPd nanosheets (Fig. S2†). The photothermal conversion efficiency (η) is calculated according to the related literature,[26] which is up to 76.6% in aqueous solution. The value of η exceeds that of most of the reported photothermal materials including noble metal nanomaterials, polymers, graphene, and MoS_2 nanosheets (Table S1†), suggesting that AuPd nanosheets may be an ideal PTT agent. The highly efficient transduction of photon energy into heat may come from the marked enhancement of the surface electromagnetic field at the tips of anisotropic nanosheets with the interaction of resonant electromagnetic radiation.[27] Photothermal stability is the other important parameter for PTT agents. AuPd nanosheets are exposed to 808 nm laser light at a power of 1 W cm^{-2} for 10 min. Then the laser is turned off and the solution is cooled for 10 min. After six cycles, the AuPd nanosheets still show a prominent photothermal effect, revealing their excellent photostability (Fig. 2d). The high value of η and outstanding photothermal stability make AuPd nanosheets promising PTT agents.

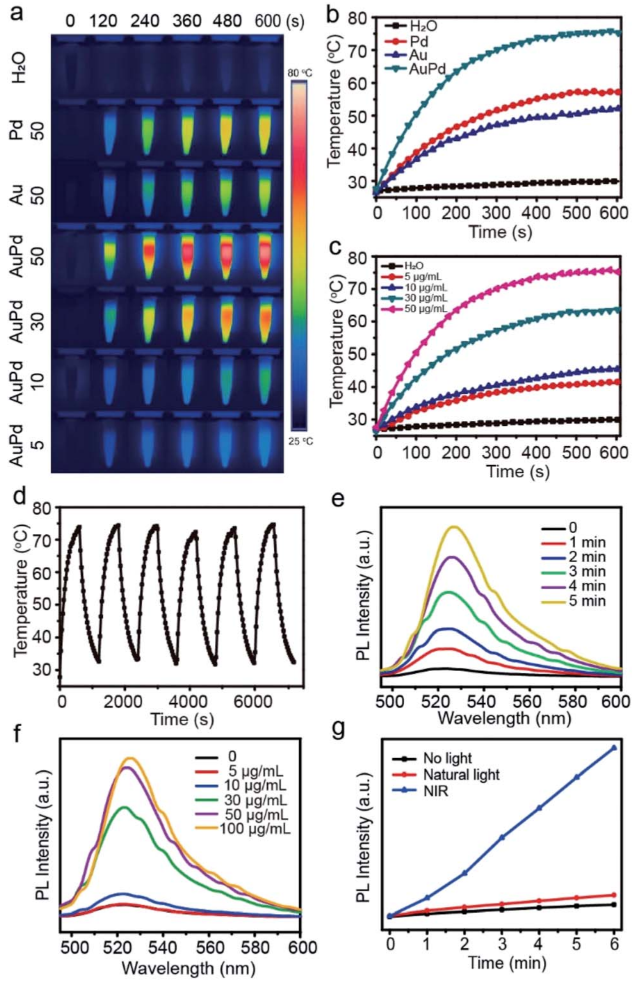

Fig. 2 Characterization of the photothermal properties and ROS generation of AuPd nanosheets. (a) Infrared thermal imaging of synthetic nanostructures with different components and concentrations (μg mL^{-1}). (b) Temperature elevation of pure Pd, Au, AuPd nanoalloy, and water irradiated using an 808 nm laser (1 W cm^{-2}). (c) Temperature elevation of AuPd nanosheets at different concentrations (0, 5, 10, 30, and 50 μg mL^{-1}) irradiated using an 808 nm laser (1 W cm^{-2}). (d) Photothermal stability of AuPd nanosheets (50 μg mL^{-1}) irradiated using an 808 nm laser (1 W cm^{-2}). (e) Fluorescence spectra of DCFH and AuPd nanosheet (50 μg mL^{-1}) mixtures under 808 nm laser irradiation (1 W cm^{-2}) for various times. (f) Fluorescence spectra of DCFH and AuPd nanosheet (0, 5, 10, 30, 50, and 100 μg mL^{-1}) mixtures under 808 nm laser irradiation (1 min, 1 W cm^{-2}). (g) Fluorescence intensity at 525 nm of DCFH and AuPd nanosheet (50 μg mL^{-1}) mixtures within 6 min under 808 nm laser irradiation (1 W cm^{-2}), natural light and darkness, respectively.

Since noble metal-based nanomaterials are reported to transform O_2 to ROS through adsorbing O_2 on the surface, possessing reactivity that resembles that of free $^1O_2$,[28] we employ 2,7-dichlorofluorescein-diacetate (DCFH-DA)[29] to evaluate the photodynamic properties of the AuPd nanosheets. Nonfluorescent DCFH exposed to ROS can be oxidized to the green fluorescent 2,7-dichlorofluorescein (DCF), probing the presence of ROS. In our experiments, the fluorescence of mixtures containing DCFH and AuPd nanosheets indicates the production of ROS and the photodynamic properties of the AuPd nanosheets. Obviously, the generation of ROS exhibits dependence on the duration of laser irradiation and the concentration of AuPd nanosheets (Fig. 2e and f). The samples irradiated using an NIR laser show remarkably higher fluorescence intensity than samples under natural light and darkness (Fig. 2g), suggesting that the AuPd nanosheets can generate ROS continually in natural light and the NIR laser irradiation can accelerate the generation of ROS significantly. Subsequently, the samples in natural light and darkness are measured every 5 min. The fluorescence increases inconspicuously in the samples shielded from light and the difference of fluorescence intensities between two samples tends to become larger gradually, which reveals that the process is typically photodynamic (Fig. S3a†). Remarkably, negligible changes in fluorescence are detected even when AuPd nanosheets are stored at room temperature in natural light over one month, showing the ideal stability of the photodynamic properties of AuPd nanosheets (Fig. S3b†). Besides, we perform electron paramagnetic resonance (EPR) measurements to determine the production of ROS including $^{\bullet}OH$, $O_2^{\bullet-}$, and $^1O_2$ (Fig. S4†). We use trapping reagents 5-dimethyl-1-pyrroline-*N*-oxide (DMPO) to trap $^{\bullet}OH$ and $O_2^{\bullet-}$, and 2,2,6,6-tetramethylpiperidine (TEMP) to trap $^1O_2$. The characteristic peaks of DMPO-$^{\bullet}OH$ and DMPO-$O_2^{\bullet-}$ indicate the production of $^{\bullet}OH$ and $O_2^{\bullet-}$ from the AuPd nanosheet solution under NIR irradiation. Meanwhile, under NIR irradiation, we find that the peak intensities of TEMP-$^1O_2$ in AuPd nanosheet solution are obviously higher than those in water, suggesting the generation of $^1O_2$.

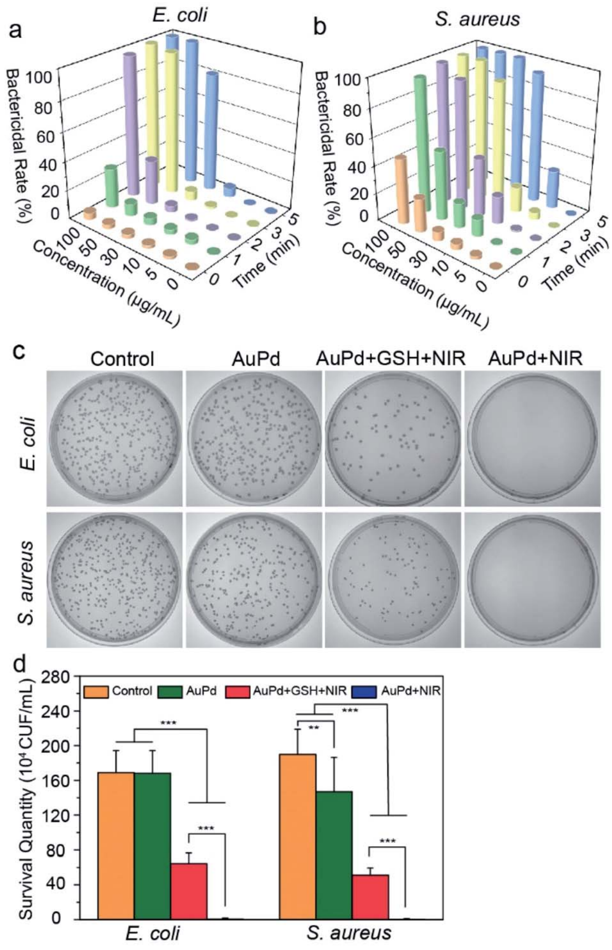

Fig. 3 *In vitro* antibacterial activity of AuPd nanosheets. (a) Antibacterial activity for *E. coli* under 1 W cm^{-2} power density, irradiation times of 0, 1, 2, 3, and 5 min, and concentrations of 0, 5, 10, 30, 50, and 100 μg mL^{-1}. (b) Antibacterial activity for *S. aureus* under 1 W cm^{-2} power density, irradiation times of 0, 1, 2, 3, and 5 min, and concentrations of 0, 5, 10, 30, 50, and 100 μg mL^{-1}. (c) Plate count method used in four groups for *E. coli* and *S. aureus* (control, AuPd, AuPd + GSH + NIR, and AuPd + NIR; concentrations of GSH and AuPd are 0.5 mg mL^{-1} and 50 μg mL^{-1}, respectively, and the power density of the 808 nm NIR laser is 1 W cm^{-2}). (d) Statistical histogram of colony numbers in four groups in (b) ($n = 6$, $^{**}P < 0.01$, $^{***}P < 0.001$).

In vitro antibacterial activity

Escherichia coli (*E. coli*) and *S. aureus* are used as the representative Gram-negative and Gram-positive bacteria to investigate the antibacterial activity of AuPd nanosheets. As hyperpyrexia and ROS production are closely related to the concentration of AuPd nanosheets, power of laser, and time of irradiation, the antibacterial effect is influenced by these parameters greatly. The decrease of bacterial survival rate is consistent with the enhancement of these parameters. Against *E. coli*, when the power of laser is 1 W cm^{-2}, the bactericidal rate is 100% with 50 μg mL^{-1} AuPd nanosheets for 5 min of irradiation, and 97.6% with 100 μg mL^{-1} AuPd nanosheets for 2 min of irradiation (Fig. 3a). With the same procedures, the antibacterial effects against *S. aureus* display a similar tendency and better results. The irradiation with 808 nm laser light at 1 W cm^{-2} for 5 min enables a bactericidal rate of 100% with 30 μg mL^{-1} AuPd nanosheets (Fig. 3b). Interestingly, the AuPd nanosheets at a concentration of 50 μg mL^{-1} can kill *S. aureus*, with a bactericidal rate of 24.7% even though no laser is turned on. We suggest two reasons for this phenomenon: one is the cationic surfactant, OTAC, used in the synthesis of AuPd nanosheets. Many cationic polymers and surfactants are effective antibacterial agents against Gram positive bacteria.[30,31] The other is that Gram positive bacteria are easy to kill by PDT, and the distinction in the susceptibility to PDT based on Gram staining comes from differences in their cell structures.[32] Gram negative bacteria have a complicated multi-layered outer barrier structure including a glycocalyx, lipopolysaccharide, outer membrane lipid bilayer, periplasm, peptidoglycan cell wall, and plasma membrane lipid bilayer, resulting in a big difference in their membrane permeability compared to Gram positive bacteria.[33,34] Although the laser is off, ROS can be produced with the help of natural light and can kill some *S. aureus*. To observe the influence of laser power, 0.5, 2, and 3 W cm^{-2} are used. At the same concentration of AuPd nanosheets, to achieve similar bactericidal effects, a longer irradiation time is required at a lower laser power and likewise a shorter irradiation time at a higher laser power (Fig. S5†). Besides bactericidal rate, minimum inhibitory concentration (MIC) and minimal bactericidal concentration (MBC) are other important factors to evaluate the bactericidal activity of antimicrobial agents against pathogens. MIC is defined as the minimal concentration of an antibacterial agent inhibiting the visible growth of a microorganism after overnight incubation, and MBC is the lowest concentration of an antibacterial agent preventing the growth of bacteria after subculture in antibiotic-free media.[35] We test the MIC and MBC under different NIR irradiation times and powers (Tables S2 and S3†). Higher MIC and MBC are obtained at a lower laser power or a shorter irradiation time. The tendency is consistent with the results of the bactericidal rate. Considering the side effects caused by the high intensity of laser and concentration of nanosheets, we choose a laser power of 1 W cm^{-2} and 50 μg mL^{-1} nanoagent concentration for subsequent experiments, which can kill 100% of pathogens covering both *E. coli* and *S. aureus*.

To verify the synergistic antibacterial effects of photothermal effects and ROS, we group the bacteria, including *E. coli* and *S. aureus*, into four classes (Fig. 3c and d). Bacteria cultured in medium act as the control group to ensure that the bacteria used in all the experiments are normal. In the AuPd + GSH + NIR group, bacteria are incubated with AuPd nanosheets and GSH (0.5 mg mL^{-1}), and irradiated using an NIR laser simultaneously. Because GSH is an important antioxidant to quench ROS,[36] it is used to eliminate the ROS generated by the photodynamic process and ensure that the antibacterial effect comes from hyperpyrexia. The colonies decrease significantly compared with the sole addition of AuPd without NIR irradiation (AuPd group), and the bactericidal rate is 62.1% for *E. coli* and 72.6% for *S. aureus*, confirming the antibacterial activity of photothermy. Furthermore, when the bacteria are incubated with AuPd nanosheets and irradiated using an NIR laser (AuPd + NIR group), no colonies grow in culture plates and compared with the AuPd + GSH + NIR group (no PDT effect), the bactericidal rate is significantly higher, 100% for both *E. coli* and *S. aureus*. The results demonstrate the synergistic antibacterial ability of PTT and PDT *in vitro*.

Targeting peptide modification of AuPd

We next endow the AuPd nanosheets with targeting property to specific bacteria through coating them with targeting peptides (AuPd@Peptide). In the proof-of-concept experiments, a cyclic 9-amino-acid peptide CARGGLKSC is introduced as it is recently reported to target *S. aureus*,[21] and the interaction between the thiol in its structure and noble metals can be used to firmly functionalize the AuPd nanosheets.[37] CARGGLKSC is an efficient targeting peptide without any antibacterial activity (MIC > 1000 μg mL^{-1}). After the functionalization, we use the infrared spectrum to verify the existence of peptides on AuPd nanosheets. In the infrared spectrum, a new peak of absorption at 1670 cm^{-1} appears, which is the representative peak of amide bonds (Fig. S6†). Besides, the peak for S2p which is a specific element of peptides in X-ray photoelectron spectroscopy (XPS) appears at 165 eV, suggesting the coating of peptides on AuPd nanosheets. UV-Vis absorption spectra (Fig. 1f) exhibit no change in the low energy region but show an apparent increase in the high energy band (≤235 nm), similar to that of the peptide. To evaluate the amount of the targeting peptide in AuPd@Peptide, we analyze the elements in samples by XPS. The proportion of Au and S is 4.6 : 1 (Fig. S7†). Because the shapes of the AuPd nanosheets are irregular, we cannot get the specific ratio of the modified peptide in the final nanomaterials as in the case of small spherical nanoparticles.[37,38] Meanwhile, we find that the photothermal and photodynamic properties of AuPd nanosheets are not influenced by the modification with the peptide (Fig. 4a and b), making them suitable for the following application.

Subsequently, the targeting property of AuPd@Peptide *in vitro* is investigated. We treat *S. aureus* with AuPd nanosheets with and without peptides and analyze the samples by scanning electron microscopy (SEM). We use *S. aureus* without any treatment as the control to ensure the normal state of bacteria (Fig. 4c and d). Scarcely AuPd nanosheets attach to the surface of *S. aureus* treated with uncoated AuPd nanosheets and only some aggregates are found (Fig. 4e and f). In contrast,

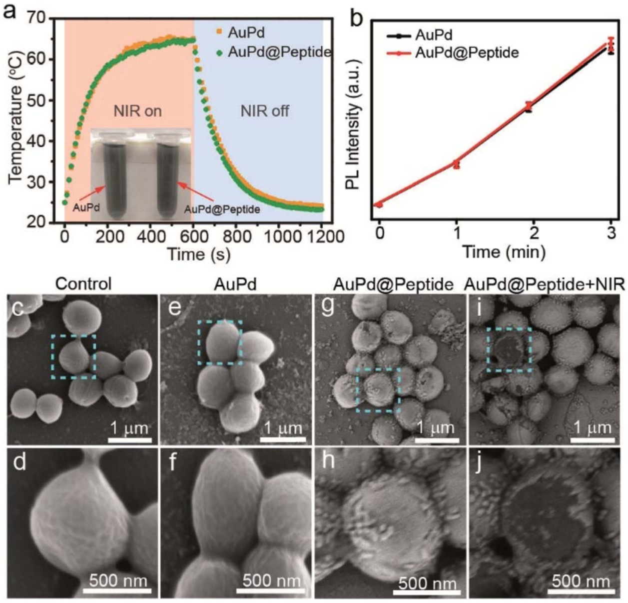

Fig. 4 Photometrics and targeting property of AuPd@Peptide. (a) Photothermal test for AuPd and AuPd@Peptide (inset photograph shows the corresponding AuPd and AuPd@Peptide aqueous solutions). (b) Photodynamic test for AuPd and AuPd@Peptide. (c and d) *S. aureus* treated with PBS, and (d) shows the region enclosed by a blue dashed square in (c). (e and f) *S. aureus* treated with AuPd, and (f) shows the region enclosed by a blue dashed square in (e). (g and h) *S. aureus* treated with AuPd@Peptide, and (h) is the region enclosed by a blue dashed square in (g). (i and j) *S. aureus* treated with AuPd@Peptide and NIR laser light (5 min, 1 W cm^{-2}), and (j) is the region enclosed by a blue dashed square in (i).

monodisperse AuPd@Peptide can stick to the surface of *S. aureus* (Fig. 4g and h), suggesting their apparent active targeting ability. Furthermore, when samples are exposed to NIR laser light, some *S. aureus* are cracked and fractured morphologically due to the damage from photothermal and photodynamic effects (Fig. 4i and j). The targeting property can make photonic nanoagents accumulate in the infected region, enhancing the efficiency of imaging and therapy *in vivo*.

Targeting imaging and phototherapies *in vivo*

Because the biocompatibility of AuPd@Peptide must be considered in the biomedical applications *in vivo*, a cytotoxicity test and hemolysis assay are performed. No obvious cytotoxicity results from the incubation of AuPd@Peptide and human umbilical vein endothelial cells (HUVEC) for 24 h. Even when the concentration of AuPd@Peptide reaches 128 μg mL^{-1}, the cell viability remains over 85% (Fig. S8a†). Meanwhile, negligible hemolysis in the presence of AuPd@Peptide is detected. The hemolysis is lower than 2.5% when the concentration of AuPd@Peptide is up to 128 μg mL^{-1} (Fig. S8b†). The distribution of AuPd@Peptide nanosheets to peripheral organs and their clearance are of paramount importance for their further *in vivo* application.[39] After treatment with an intravenous dose of AuPd@Peptide (2 mg mL^{-1}, 100 μL), the Au levels in the wound and major organs are measured by ICP-MS. As illustrated in Fig. S9, the liver and spleen have higher concentration of AuPd@Peptide similar to some reported nanomaterials,[40] and about 80% of nanomaterials can be excreted after 36 h, suggesting no significant metal residues. Moreover, a blood test of mice is executed at the 7th day after the tail intravenous injection of AuPd@Peptide (2 mg mL^{-1}, 100 μL), and no significant change in biomedical health indicators is caused (Table S4†), which reveals that AuPd@Peptide nanosheets cause no impact on the blood circulation and hepatic and renal functions of mice.[41] All these results suggest the good biocompatibility of AuPd@Peptide nanosheets and promise their potential application *in vivo*.

Although some noble metal nanoparticles, such as silver and gold, can kill bacteria without the assistance of photon,[42–44] all of them cannot realize imaging guided therapy *in vivo*. Thermal expansion can generate acoustic signals, making many photothermal agents with optical absorption act as photoacoustic contrast agents simultaneously. We find that AuPd nanosheets can generate concentration dependent PA signals as well (Fig. S10†). Mouse models of subcutaneous abscess caused by *S. aureus* are used in PAI *in vivo*. After the intravenous injection of AuPd@Peptide (2 mg mL^{-1}, 100 μL), gradually enhanced PA signals are recorded over time, which is helpful in monitoring the real-time accumulation of AuPd@Peptide in the infected region with high spatial resolution. After 1 h of injection, the apparent accumulation of AuPd@Peptide is in the interface of corium and subcutis (red dotted circles in Fig. 5a) which is the area of infection, indicating the targeting property *in vivo*. At 4 h after injection, PA signals reach the maximum. Then signals start attenuation and decrease to the initial level within 36 h. The intensities of PA signals in the infected region also prove the imaging performance (Fig. S11†). According to the results of PAI, we can introduce laser light at the most accurate time and get the best therapeutic effect.

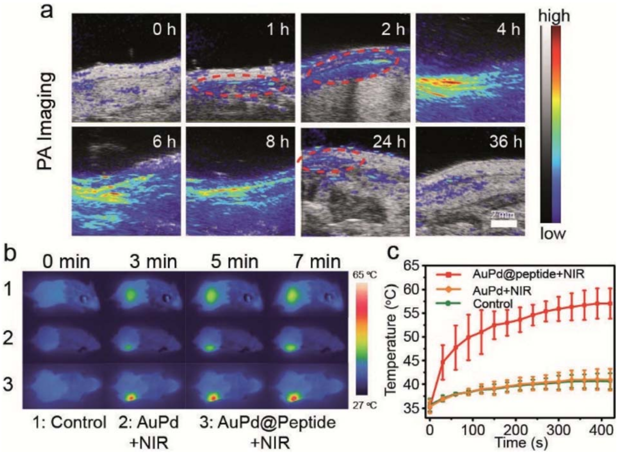

Fig. 5 PA and PT imaging of *S. aureus* infected subcutaneous abscess in mice. (a) PAI of the infected region after intravenous injection of 100 μL of AuPd@Peptide nanosheets (2 mg mL^{-1}), the scale bar is 2 mm. (b) Infrared thermal images of the infected regions 4 h after the injection of AuPd@Peptide with irradiation for different times. (c) Temperature of the infected regions with the increase of irradiation time.

Guided by PAI, the infrared thermal imaging of AuPd@Peptide *in vivo* is further studied under 808 nm laser irradiation (1 W cm^{-2}) 4 h after injection, ensuring the maximum accumulation in infected regions. The thermal imaging shows that the temperature in the infected areas of AuPd@Peptide injected mice increases rapidly, showing a giant difference compared with the control and the AuPd group with irradiation for the same time (Fig. 5b). The temperature is ~55.9 °C at 5 min after irradiation and reaches a plateau of ~57.0 °C averagely at 7 min, compared with the ~40.6 °C in the control and AuPd groups, suggesting the remarkable active bacteria targeting performance and photothermal effect of AuPd@Peptide *in vivo* (Fig. 5c).

Motivated by the excellent PAI effects, photothermal conversion ability, and ROS production of AuPd@Peptide, the PAI guided photonic therapy of bacterial infection is performed *in vivo*. The mice with *S. aureus* caused subcutaneous abscess are randomly divided into three groups, including the control group (using PBS), only AuPd@Peptide treated group, and the group treated with AuPd@Peptide combined with NIR irradiation, respectively. In the last group, mice are irradiated using 808 nm laser light 4 h after the intravenous injection of AuPd@Peptide (2 mg mL^{-1}, 100 μL) according to the PAI results, ensuring the adequate accumulation of AuPd@Peptide in the infected regions. At 3 days after treatment, the group treated with AuPd@Peptide with the assistance of NIR heal faster apparently and the areas of wounds display a more significant difference at the 6th day. Finally, the wounds almost disappear 12 days after the treatment, while the unhealed parts are still more than 20% of original wounds in the control and AuPd@Peptide groups (Fig. 6a and b). The results indicate that the treatment of bacterial infection in the early stage of wounds

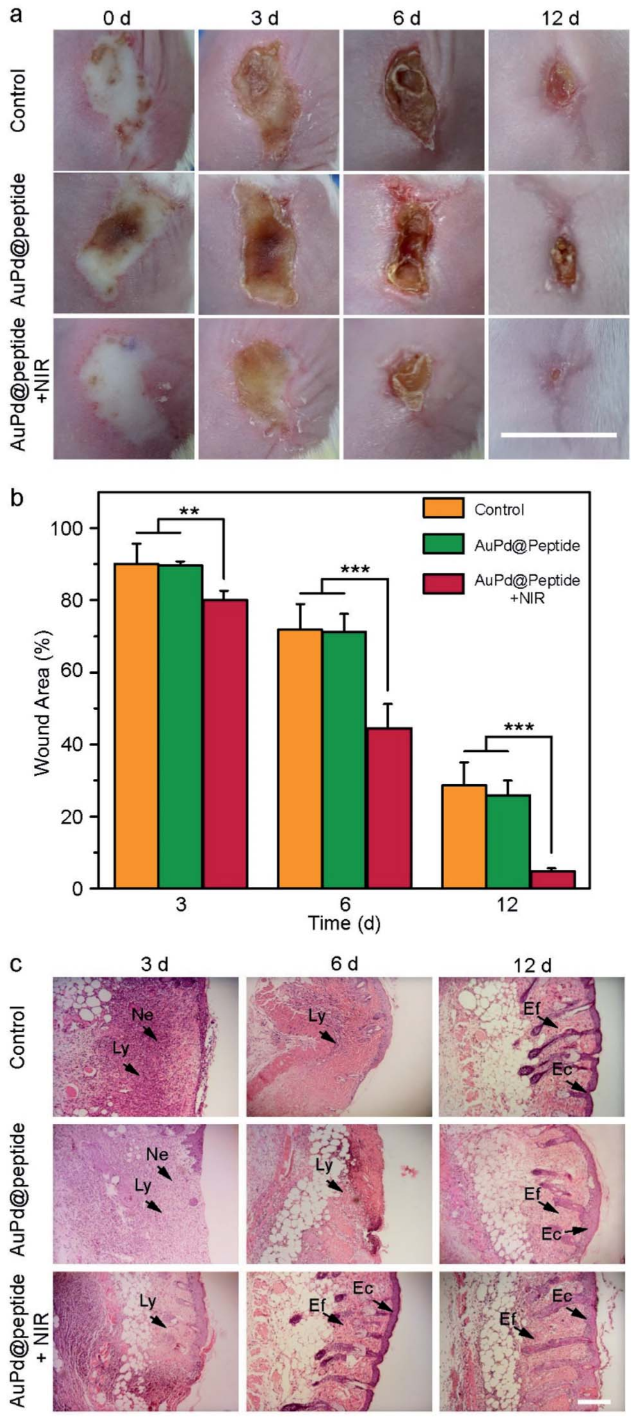

Fig. 6 Antibacterial and wound-healing experiment *in vivo*. (a) Representative photographs of *S. aureus* infected subcutaneous abscess in 3 different treatment groups (PBS, AuPd@Peptide, and AuPd@Peptide plus NIR) within 12 days. NIR laser irradiation (808 nm, 1 W cm^{-2}, 5 min) is employed. Scale bars are 1 cm. (b) Corresponding areas of infected wounds presented in (a) ($^{**}p < 0.01$; $^{***}p < 0.001$). (c) H&E staining of skin tissues of *S. aureus* infected mouse wounds on days 3, 6, and 12. Scale bars are 500 μm (Ly, lymphocytes; Ne, neutrophils; Ec, epithelial cells; Ef, elongated fibroblasts).

can promote their closure, consistent with the described systems.[45,46] The tissues of wounded skins are stained using hematoxylin and eosin (H&E) (Fig. 6c). Bacteria-infected wounds lack epithelial layers and show invaded lymphocytes and neutrophils, implying the occurrence of inflammation. The appearance of elongated fibroblasts and epithelial cells demonstrates the process of healing, because elongated fibroblasts can influence the formation of collagen, and epithelial cells are important parts in the skin.[47] With time, in the AuPd@Peptide plus NIR treated group, lymphocytes and neutrophils disappear and elongated fibroblasts and epithelial cells appear sooner than the other two groups. All results verify that the photonic effects of AuPd@Peptide can promote the healing of wounds.

Conclusions

We have developed a one-step strategy to synthesize 2D AuPd nanosheets for PAI-guided photonic antibacterial nanomedicine. AuPd nanosheets exhibit prominent photothermal effects ($\eta = 76.6\%$) under NIR irradiation. The combination of PTT and PDT facilitates rapid and efficient bactericidal effects at low temperature and moderate ROS generation which guarantees good biocompatibility. Targeting peptide modified AuPd nanosheets further realize PAI-guided precise PTT and PDT for infection caused by *S. aureus* in mice. The promotion of the healing of infected wounds validates the remarkable photonic sterilizing effects of AuPd nanosheets *in vivo*. Our study broadens the biomedical application of 2D noble metal nanomaterials as photonic nano-antibiotics. Besides, according to our results, another class of intriguing 2D monoelemental materials (Xenes) presenting unique photonic properties may have potential to be applied as photonic nano-antibiotics as well.[48–54] The straightforward synthesis process, the convenient application of a single laser, and the prominent antimicrobial abilities would simplify the future application.

Experimental

Materials

Chloroauric acid ($HAuCl_4$), palladium chloride ($PdCl_2$), 2′,7′-dichlorodihydrofluorescein diacetate (DCFH-DA), sodium ascorbate, EDTA anticoagulant, and glutathione were purchased from Sigma-Aldrich. Octadecyl trimethyl ammonium chloride (OTAC), hydrochloric acid (36–38%), NaOH, and NaCl were received from Sinopharm Chemical Reagent Co. Ltd. Phosphate buffered saline (PBS) and agar medium were received from Sangon Biotech Co. Ltd. CCK-8 assay was from Beyotime Institute of Biotechnology. Biomedical health indicator assay kits were provided by Icubio.

Apparatus

Fluorescence data were obtained from a Lumina fluorescence spectrophotometer (Thermo Fisher). Excitation and emission slit widths were both 5 nm. Atomic force microscopy (AFM) images were recorded using a Dimension ICON (Bruker). The UV-Vis absorption spectrum was measured using a SHIMADZU UV-1780 UV-Vis spectrophotometer. X-ray diffraction analysis (XRD) was carried out using an X-ray diffractometer (D8

Advance, Bruker). The infrared spectrum was recorded on a Spectrum Two FT-IR spectrometer (Perkin Elmer). Transmission electron microscopy (TEM) images were obtained by using a Tecnai F30 at an accelerating voltage of 300 kV. The laser light was supplied by a fiber-coupled continuous semiconductor diode laser (KS-810F-8000, Kai Site Electronic Technology Co. Ltd.), and the temperature was measured using a fixed-mounted thermal imaging camera (FLIR A300-series). Photoacoustic signals were recorded using a photoacoustic computed tomography scanner (Vevo LAZR, FUJIFILM VisualSonics). ICP-MS was performed using a Perkin Elmer instrument (NexIon300X). Routine laboratory blood tests were performed on a blood cell analyzer (BC-31s, Mindray), and the indicators of hepatic and renal functions were tested using a biochemical analyzer (iMagic-M7, Icubio). Optical densities were obtained from a microplate reader (BioTek Synergy H1). Photographs were taken using a commercial camera (SONY, ILCE-6000L).

Synthesis and modification of AuPd nanosheets

In a typical synthesis, 0.3 mL of H_2PdCl_4 (0.01 M) and 0.7 mL of $HAuCl_4$ (0.01 M) were sequentially added to 50 mL of OTAC aqueous solution (0.01 M). After bath-sonication for 10 min, to the solution was added 1 mL of sodium ascorbate solution (20 mg mL^{-1}) under agitation at 500 rpm and allowed to react at room temperature for 4 h without agitation. Alloys with different compositions could be obtained by varying the feed ratio of Au/Pd. Pure Au and Pd nanosheets were collected under the same conditions but without H_2PdCl_4 and $HAuCl_4$, respectively. Solid products were collected by centrifugation at 12 000 rpm and washed two times with water. After drying, the solid products were stored at 4 °C. They were re-dispersed in pure water or PBS and used to prepare different solutions of various concentrations according to the demand.

For the modification of AuPd nanosheets, 1.5 mg of AuPd nanosheets were dispersed in 10 mL of pure water and 1 mL of targeting peptide solution (1 mg mL^{-1}) was added. After 24 h (agitation at 200 rpm, room temperature), the products were collected by centrifugation at 10 000 rpm and washed with water once. Modified AuPd nanosheets were re-dispersed in PBS for further experiments.

NIR photothermal and photodynamic effects

To investigate the photothermal effect of AuPd nanosheets, aqueous suspensions of AuPd at different concentrations (0, 5, 10, 30, and 50 μg mL^{-1}) were added to EP tubes (Eppendorf). Then the samples were irradiated with an 808 nm NIR laser (1.0 W cm^{-2}) for 600 s and the temperature was recorded every 10 s using a thermal imaging camera. Control experiments with products of different components were carried out under the same irradiation conditions and the concentration was 50 μg mL^{-1}.

ROS generation was detected using a chemical probe, 2,7-dichlorofluorescein (DCFH). In a feasible procedure, DCFH formed after continuous stirring of a mixed solution containing methanol solution of DCFH-DA (1 mL, 1 mM) and NaOH (1 mL, 0.01 M) for 30 min in the dark. Subsequently, moderate PBS (pH = 7) was added to the above solution to adjust the pH to be neutral. The AuPd nanosheets were mixed with DCFH and irradiated with 808 nm NIR light under different conditions. The fluorescence spectra of the tested solutions were recorded using a spectrofluorometer at an excitation wavelength of 488 nm.

Calculation of photothermal conversion efficiency of AuPd

According to Roper's report, the photothermal conversion efficiency (η) of AuPd was calculated using the following equation,[26]

$$\eta = \frac{hS(T_{\max} - T_{\text{surr}}) - Q_{\text{Dis}}}{I(1 - 10^{-A_{808}})} \tag{1}$$

where h (mW (m^{-2} °C^{-1})) is the heat transfer coefficient, S (m^2) is the surface area of the container, $T_{\max}$ (°C) is the equilibrium temperature, and T_{surr} (°C) is the ambient temperature of the surroundings. In this experiment, $T_{\max} - T_{\text{surr}}$ was 50.8 °C according to Fig. S3.† Q_{Dis} (mW) expresses the heat absorption of the EP tube and it was 8.80 mW independently measured using an EP tube containing pure water. I represents the incident laser power (1 W) and A_{808} is the absorbance of AuPd at 808 nm (0.586).

To get hS, a time constant τ_s in the spontaneous cooling system is introduced,

$$\tau_s = \frac{\sum_i m_i C_{p,i}}{hS} \tag{2}$$

$$t = \tau_s \ln(\theta) \tag{3}$$

t is the cooling time and θ is the temperature-related variable,

$$\theta = \frac{T - T_{\text{surr}}}{T_{\max} - T_{\text{surr}}} \tag{4}$$

T is the temperature corresponding to time point (t); τ_s was determined to be 370.28 s (Fig. S3†), and thus hS was deduced to be 11.34 mW °C^{-1} (substituting $m = 1$ g, $C = 4.2$ J (g^{-1} °C^{-1}) in eqn (2)).

Finally, the photothermal conversion efficiency (η) of AuPd was calculated to be 76.6% from eqn (1).

EPR

We made use of paramagnetic trapping reagents 5-dimethyl-1-pyrroline *N*-oxide (DMPO) to trap $O_2^{\bullet -}$ and $^{\bullet}OH$, and 2,2,6,6-tetramethylpiperidine (TEMP) to trap $^1O_2$.[55] We mixed AuPd nanosheets (200 μg mL^{-1}) with the paramagnetic trapping reagents (200 mM) (v/v = 1 : 1) and used an 808 nm laser to irradiate the solution for 5 min at 1 W cm^{-2}. DI water with laser irradiation in the presence of paramagnetic trapping agents was applied as the control. We recorded EPR spectra in capillary tubes at a microwave frequency of 9.84 GHz, a microwave power of 2 mW, a center field of 3514 G, a sweep width of 200 G, a time constant of 0.01 ms, a modulation frequency of 100 kHz, and a modulation width 1.00 G.

Bacterial culture

To obtain bacterial solutions, a single colony of *E. coli* or *S. aureus* cultured on an agar plate was transferred to 1 mL of broth medium and put in a constant temperature shaking bed at 37 °C and shaken at a speed of 200 rpm for 4–5 h. The bacterial solution was diluted to an optical density of 0.1 at 600 nm detected using a UV-Vis spectrophotometer ($\mathrm{OD}_{600} = 0.1$, 2.8×10^9 CFU mL^{-1} for *E. coli* and 2.0×10^8 CFU mL^{-1} for *S. aureus*) with PBS for antibacterial evaluation.

NIR triggered phototherapies *in vitro*

125 μL of $\sim 10^6$ CFU mL^{-1} bacterial PBS solutions (*E. coli* or *S. aureus*) and 125 μL of solutions with different concentrations of AuPd nanosheets were added to 96-well plates. The final concentrations of AuPd nanosheets were 0, 5, 10, 30, 50, and 100 μg mL^{-1}, respectively. Then the antibacterial effects of phototherapies were tested under different irradiation power densities (0.5, 1, 2, and 3 W cm^{-2}) and times (0, 1, 2, 3, and 5 min), respectively. The antibacterial results were evaluated using the bacterial survival rate or bactericidal rate. After different treatments, 50 μL of the bacterial solution in 96-well plates was transferred to an agar plate and scattered homogeneously. Bacterial colonies were counted after cultivation for 24 h at 37 °C, and the bacterial survival rate was calculated using the colony ratio of the treated group and the control group, and the bactericidal rate was one minus the value of the bacterial survival rate.

The MIC of AuPd nanosheets was measured by mixing bacteria and AuPd nanosheets (final concentrations are 100, 95, 90, …, 10, 5, and 0 μg mL^{-1}) under different laser powers (0.5, 1, 2, and 3 W cm^{-2}) and irradiation times (1, 2, 3, and 5 min), and then incubating the mixture at 37 °C for 16–20 h. The minimum concentration of AuPd nanosheets inhibiting the visible growth of the bacteria is the MIC.

The MBC of AuPd nanosheets was tested by mixing bacteria and AuPd nanosheets (final concentrations are 100, 95, 90, …, 10, 5, and 0 μg mL^{-1}) under different laser powers (0.5, 1, 2, and 3 W cm^{-2}) and irradiation times (1, 2, 3, and 5 min), and then subculturing the bacteria in an antibiotic-free agar plate for 16–20 h. The minimum concentration of AuPd nanosheets preventing the growth of the subcultured bacteria is the MBC.

Morphology observation of bacteria

Bacteria were cultured to the log phase, collected after centrifugation at 8000 rpm for 5 min, and washed once with PBS. Sterile coverslips were placed in a 24-well sterile cell culture plate and covered with 500 μL of 1×10^4 CFU mL^{-1} bacterial solution. The plate was put in an incubator with a constant temperature of 37 °C for one night. The solution of bacteria was discarded, and AuPd and AuPd@Peptide were added in different wells, respectively, to incubate with bacteria in a 37 °C incubator. The control group was added with PBS. After 4 hours, we removed the solution and washed the coverslips using PBS once. 500 μL of glutaraldehyde fixing solution (2.5%) was added to each well and the bacteria on the coverslips were fixed overnight. After that, the coverslips were washed with PBS three times and the bacteria on the coverslips were dehydrated with 30%, 50%, 70%, 95%, and 100% ethanol, respectively, for 15 min in each step. Finally, the ethanol was volatilized at room temperature, and the samples were dried naturally for further SEM analysis.

Cytotoxicity assay

HUVEC cells were cultured in Dulbecco's modified Eagle medium (DMEM) containing 10% fetal bovine serum. HUVEC cells at 1×10^4 cells per well were incubated in 96-well plates with AuPd@Peptide (0, 4, 8, 16, 32, 64, and 128 μg mL^{-1}) in 200 μL of medium for 24 hours. The supernatant was discarded, the cells were washed with PBS (0.01 M, pH 0.7), and 10% (v/v) of CCK-8 solution was added and incubated at 37 °C for 2 h. The absorbance at 450 nm determined the results, using that at 650 nm as reference.

Hemolysis assay

Fresh mouse blood was used in the hemolysis assay. Erythrocytes were obtained by centrifugation at 3000 rpm for 15 min and they were washed 3 times with saline. Erythrocytes in 1 mL of blood were dispersed in 3 mL of saline for further tests eventually. 1 mL of AuPd@Peptide nanosheets dispersed in saline at concentrations of 4, 16, 64, and 128 μg mL^{-1} were mixed with 100 μL of erythrocytes, and incubated for 30 min at 37 °C. Finally, pictures were recorded, suspensions were centrifuged at 12 000 rpm for 5 min, and UV-Vis absorption at 540 nm of supernatants was measured. Saline was used as the negative control and pure water was introduced as the positive control. The percentage of hemolysis was calculated as below,

$$\text{Hemolysis }(\%) = (A_\mathrm{s} - A_\mathrm{n})/(A_\mathrm{p} - A_\mathrm{n}) \times 100\% \tag{5}$$

in which A_s is the absorbance of the sample, A_n is the absorbance of the negative control, and A_p is the absorbance of the positive control.

Evaluation of biomedical health indicators in blood of mice

Mice were divided randomly into 2 groups ($N = 5$ per group), and were injected intravenously with 100 μL of PBS (as control, group 1) and 100 μL of 2 mg mL^{-1} AuPd@Peptide (as experimental, group 2). After 7 days, fresh mouse blood or serum was used in laboratory tests. In typical procedures of routine blood tests, 50 μL of fresh blood was mixed with 5 μL of EDTA anticoagulant and the mixed samples were analyzed using a blood cell analyzer. Indicators of hepatic and renal functions were estimated using mouse serum. In each test, 0.5 mL of serum were analyzed using a biochemical analyzer.

PAI *in vitro*

AuPd nanosheets of different concentrations were added in 200 μL EP tubes with no air bubbles in the bottom. Next, each sample was set under water and analyzed using a photoacoustic computed tomography scanner.

Mice with subcutaneous abscess caused by *S. aureus*

All animals were purchased from the Guangdong Medical Laboratory Animal Center. All animal procedures were performed in accordance with the Guidelines for Care and Use of Laboratory Animals of Shenzhen University and approved by the Animal Ethics Committee of Shenzhen University Health Science Center. A skin infection (subcutaneous abscess) model was obtained by inoculating female BALB/c mice (6 weeks; ∼20 g) with a subcutaneous injection of 100 μL of *S. aureus* supernatant ($OD_{600} = 0.1$) in the shaved right flank. After one day of inoculation, the infected mice were used in the following experiments.

PA and photothermal imaging *in vivo*

Infected mice were treated with 100 μL of AuPd@Peptide solution (2 mg mL^{-1}) by intravenous injection. PA images of infected sites were recorded at different times, which included the point of time before injection and different hours after injection (1, 2, 4, 6, 8, 24, and 36 h). Images of PAI *in vivo* were obtained from a photoacoustic computed tomography scanner. In photothermal imaging *in vivo*, infected mice were treated similarly to those in PA imaging, and the infected sites in mice were irradiated with 808 nm laser light (1 W cm^{-2}) 4 h after the injection of AuPd@Peptide. At the same time, thermal images with time change were recorded every 10 s using a thermal imaging camera.

Biodistribution of AuPd@Peptide

After injected with 100 μL of 2 mg mL^{-1} AuPd@Peptide, the mice were sacrificed at 1, 4, 8, 24, and 36 h to obtain the major organs and wound tissue. At every point, there were 3 mice in each group. After that, the organs were weighed and dissolved using aqua regia for distribution studies. ICP-MS was used to measure the quantity of Au in all samples.

Photonic therapies of infection *in vivo*

The infected mice were divided into three groups (15 mice per group, 6 for photographs and 9 for tissue analysis at 3 different times) randomly, including the control group (using PBS), only AuPd@peptide treated group, and the group treated with AuPd@peptide combined with NIR irradiation, respectively. In the last two groups, the mice were injected with 200 μg of AuPd@Peptide (about 10 mg kg^{-1}) intravenously. In the last group, 5 min of NIR irradiation (808 nm) at 1 W cm^{-2} was introduced simultaneously. Photographs of all infected mice in the experimental process were recorded. At 3, 6, and 12 days after treatment, specimens covering the entire wound and the surrounding normal tissue were harvested, dipped in 4% paraformaldehyde, embedded, sliced, stained with H&E, and recorded using a microscope.

Statistical analysis

The data were presented in the form of mean ± standard deviation for each sample. ImageJ was used to analyze the images. OriginPro 8 was used to plot graphs. Microsoft Excel 2013 was used to calculate mean values and standard deviations. Each experiment includes at least three replicates.

Conflicts of interest

There are no conflicts to declare.

Acknowledgements

We acknowledge the funding received from the National Natural Science Foundation of China (81701789, 81702102), Shenzhen Basic Research Project (JCYJ20170818144006925, JCYJ20170307153359306), and Medical Research Foundation in Guangdong Province (A2018154). We are also thankful for the help from the Instrumental Analysis Center of Shenzhen University in characterization.

References

1 K. E. Jones, N. G. Patel, M. A. Levy, A. Storeygard, D. Balk, J. L. Gittleman and P. Daszak, *Nature*, 2008, **451**, 990–993.
2 R. Dantes, Y. Mu, R. Belflower, D. Aragon, G. Dumyati, L. H. Harrison, F. C. Lessa, R. Lynfield, J. Nadle, S. Petit, S. M. Ray, W. Schaffner, J. Townes and S. Fridkin, M. S. I. Emerging Infections Program-Active Bacterial Core Surveillance, *JAMA Intern. Med.*, 2013, **173**, 1970–1978.
3 C. A. Arias and B. E. Murray, *N. Engl. J. Med.*, 2009, **360**, 439–443.
4 T. Wang, X. Zhang, L. Mei, D. Ma, Y. Liao, Y. Zu, P. Xu, W. Yin and Z. Gu, *Nanoscale*, 2020, **12**, 8415–8424.
5 X. Zhao, Y. Jia, J. Li, R. Dong, J. Zhang, C. Ma, H. Wang, Y. Rui and X. Jiang, *ACS Appl. Mater. Interfaces*, 2018, **10**, 29398–29406.
6 J.-W. Xu, K. Yao and Z.-K. Xu, *Nanoscale*, 2019, **11**, 8680–8691.
7 C. Mao, Y. Xiang, X. Liu, Y. Zheng, K. W. K. Yeung, Z. Cui, X. Yang, Z. Li, Y. Liang and S. Zhu, *ACS Appl. Mater. Interfaces*, 2019, **11**, 17902–17914.
8 S. S. Lucky, K. C. Soo and Y. Zhang, *Chem. Rev.*, 2015, **115**, 1990–2042.
9 T. Dai, Y.-Y. Huang and M. R. Hamblin, *Photodiagnosis Photodyn. Ther.*, 2009, **6**, 170–188.
10 D. Gao, X. Ji, J. Wang, Y. Wang, D. Li, Y. Liu, K. Chang, J. Qu, J. Zheng and Z. Yuan, *J. Mater. Chem. B*, 2018, **6**, 732–739.
11 T. Kim, Q. Zhang, J. Li, L. Zhang and J. V. Jokerst, *ACS Nano*, 2018, **12**, 5615–5625.
12 Z. Guo, S. Zhu, Y. Yong, X. Zhang, X. Dong, J. Du, J. Xie, Q. Wang, Z. Gu and Y. Zhao, *Adv. Mater.*, 2017, **29**, 1704136.
13 Z. Hu, C. Wang, F. Zhao, X. Xu, S. Wang, L. Yu, D. Zhang and Y. Huang, *Nanoscale*, 2017, **9**, 8825–8833.
14 Y. Cai, Z. Wei, C. Song, C. Tang, W. Han and X. Dong, *Chem. Soc. Rev.*, 2019, **48**, 22–37.
15 T. T. Cai, G. Fang, X. Tian, J. J. Yin, C. Y. Chen and C. C. Ge, *ACS Nano*, 2019, **13**, 12694–12702.
16 X. Huang, S. Tang, X. Mu, Y. Dai, G. Chen, Z. Zhou, F. Ruan, Z. Yang and N. Zheng, *Nat. Nanotechnol.*, 2011, **6**, 28–32.

17 X. Yang, M. Yang, B. Pang, M. Vara and Y. Xia, *Chem. Rev.*, 2015, **115**, 10410–10488.
18 W. Chen, S. Zhang, Y. Yu, H. Zhang and Q. He, *Adv. Mater.*, 2016, **28**, 8567–8585.
19 M. Chen, S. Tang, Z. Guo, X. Wang, S. Mo, X. Huang, G. Liu and N. Zheng, *Adv. Mater.*, 2014, **26**, 8210–8216.
20 A. J. McGrath, Y. H. Chien, S. Cheong, D. A. Herman, J. Watt, A. M. Henning, L. Gloag, C. S. Yeh and R. D. Tilley, *ACS Nano*, 2015, **9**, 12283–12291.
21 S. Hussain, J. Joo, J. Kang, B. Kim, G. B. Braun, Z.-G. She, D. Kim, A. P. Mann, T. Mölder and T. Teesalu, *Nat. Biomed. Eng.*, 2018, **2**, 95–103.
22 J. Lai, Y. Chao, P. Zhou, Y. Yang, Y. Zhang, W. Yang, D. Wu, J. Feng and S. Guo, *Electrochem. Energy Rev.*, 2018, **1**, 531–547.
23 L. Zhang, J. Zhang, Q. Kuang, S. Xie, Z. Jiang, Z. Xie and L. Zheng, *J. Am. Chem. Soc.*, 2011, **133**, 17114–17117.
24 X. Huang, Z. Zhao, L. Cao, Y. Chen, E. Zhu, Z. Lin, M. Li, A. Yan, A. Zettl and Y. M. Wang, *Science*, 2015, **348**, 1230–1234.
25 P. K. Jain, X. Huang, I. H. El Sayed and M. A. El Sayed, *Acc. Chem. Res.*, 2008, **41**, 1578–1586.
26 Y. Liu, D. D. Wang, L. Zhao, M. Lin, H. Z. Sun, H. C. Sun and B. Yang, *RSC Adv.*, 2016, **6**, 15854–15860.
27 Z. Liu, L. Cheng, L. Zhang, Z. Yang, Z. Liu and J. Fang, *Biomaterials*, 2014, **35**, 4099–4107.
28 R. Long, H. Huang, Y. Li, L. Song and Y. Xiong, *Adv. Mater.*, 2015, **27**, 7025–7042.
29 M. U. Farid, S. Jeong, D. H. Seo, R. Ahmed, C. Lau, N. K. Gali, Z. Ning and A. K. An, *Nanoscale*, 2018, **10**, 4475–4487.
30 H. J. Jian, R. S. Wu, T. Y. Lin, Y. J. Li, H. J. Lin, S. G. Harroun, J. Y. Lai and C. C. Huang, *ACS Nano*, 2017, **11**, 6703–6716.
31 K. R. Sims, Y. Liu, G. Hwang, H. I. Jung, H. Koo and D. S. Benoit, *Nanoscale*, 2019, **11**, 219–236.
32 T. Demidova and M. Hamblin, *Int. J. Immunopathol. Pharmacol.*, 2004, **17**, 245–254.
33 R. E. Hancock, *Trends Microbiol.*, 1997, **5**, 37–42.
34 M. Vaara, *Microbiol. Mol. Biol. Rev.*, 1992, **56**, 395–411.
35 J. M. Andrews, *J. Antimicrob. Chemother.*, 2001, **48**, 5–16.
36 S. Liu, T. H. Zeng, M. Hofmann, E. Burcombe, J. Wei, R. Jiang, J. Kong and Y. Chen, *ACS Nano*, 2011, **5**, 6971–6980.
37 Y. Zhao, Y. Tian, Y. Cui, W. Liu, W. Ma and X. Jiang, *J. Am. Chem. Soc.*, 2010, **132**, 12349–12356.
38 Y. Feng, W. Chen, Y. Jia, Y. Tian, Y. Zhao, F. Long, Y. Rui and X. Jiang, *Nanoscale*, 2016, **8**, 13223–13227.
39 J. Bourquin, A. Milosevic, D. Hauser, R. Lehner, F. Blank, A. Petri Fink and B. Rothen Rutishauser, *Adv. Mater.*, 2018, **30**, 1704307.
40 K. Ma, Y. Li, Z. Wang, Y. Chen, X. Zhang, C. Chen, H. Yu, J. Huang, Z. Yang and X. Wang, *ACS Appl. Mater. Interfaces*, 2019, **11**, 29630–29640.
41 P. Zhao, Z. Jin, Q. Chen, T. Yang, D. Chen, J. Meng, X. Lu, Z. Gu and Q. He, *Nat. Commun.*, 2018, **9**, 1–12.
42 Z.-m. Xiu, Q.-b. Zhang, H. L. Puppala, V. L. Colvin and P. J. Alvarez, *Nano Lett.*, 2012, **12**, 4271–4275.
43 K. Zheng, M. I. Setyawati, D. T. Leong and J. Xie, *ACS Nano*, 2017, **11**, 6904–6910.
44 K. Zheng, M. I. Setyawati, D. T. Leong and J. Xie, *Coord. Chem. Rev.*, 2018, **357**, 1–17.
45 Z. Sun, W. Zheng, G. Zhu, J. Lian, J. Wang, P. Hui, S. He, W. Chen and X. Jiang, *ACS Appl. Mater. Interfaces*, 2019, **11**, 45381–45389.
46 X. Ren, C. Yang, L. Zhang, S. Li, S. Shi, R. Wang, X. Zhang, T. Yue, J. Sun and J. Wang, *Nanoscale*, 2019, **11**, 11830–11838.
47 W. L. Garner, *Plast. Reconstr. Surg.*, 1998, **102**, 135–139.
48 N. Kong, X. Ji, J. Wang, X. Sun, G. Chen, T. Fan, W. Liang, H. Zhang, A. Xie, O. C. Farokhzad and W. Tao, *Nano Lett.*, 2020, **20**, 3943–3955.
49 Z. Tang, N. Kong, J. Ouyang, C. Feng, N. Y. Kim, X. Ji, C. Wang, O. C. Farokhzad, H. Zhang and W. Tao, *Matter*, 2020, **2**, 297–322.
50 W. Tao, N. Kong, X. Ji, Y. Zhang, A. Sharma, J. Ouyang, B. Qi, J. Wang, N. Xie and C. Kang, *Chem. Soc. Rev.*, 2019, **48**, 2891–2912.
51 W. Tao, X. Ji, X. Zhu, L. Li, J. Wang, Y. Zhang, P. E. Saw, W. Li, N. Kong and M. A. Islam, *Adv. Mater.*, 2018, **30**, 1802061.
52 W. Tao, X. Ji, X. Xu, M. A. Islam, Z. Li, S. Chen, P. E. Saw, H. Zhang, Z. Bharwani and Z. Guo, *Angew. Chem., Int. Ed.*, 2017, **56**, 11896–11900.
53 J. Ouyang, C. Feng, X. Ji, L. Li, H. K. Gutti, N. Y. Kim, D. Artzi, A. Xie, N. Kong, Y. N. Liu, J. G. Tearney, X. Sui, W. Tao and C. O. Farokhzad, *Angew. Chem.*, 2019, **131**, 13539–13544.
54 X. Ji, Y. Kang, J. Ouyang, Y. Chen, D. Artzi, X. Zeng, Y. Xiao, C. Feng, B. Qi, N. Y. Kim, P. E. Saw, N. Kong, C. O. Farokhzad and W. Tao, *Adv. Sci.*, 2019, **6**, 1901211.
55 R. Zhang, Y. Li, M. Zhou, C. Wang, P. Feng, W. Miao and H. Huang, *ACS Appl. Mater. Interfaces*, 2019, **11**, 26711–26721.